

1 **Contrasting Aerosol Mixing States at Inland and Coastal Sites: An**
2 **Entropy-Based Metric for CCN Activity**

3 Jingye Ren^{1,2}, Wei Xu³, Ru-Jin Huang^{1*}, Fang Zhang^{4*}, Ying Wang¹, Lu Chen⁵, Jurgita
4 Ovadnevaite⁶, Darius Ceburnis⁶, Colin O'Dowd⁶, Yele Sun⁷

5 *¹State Key Laboratory of Loess Science, Institute of Earth Environment, Chinese*
6 *Academy of Sciences, Xi'an, 710061, China,*

7 *²Xi'an Institute for Innovative Earth Environment Research, Xi'an, 710061, China,*

8 *³State Key Laboratory of Advanced Environmental Technology, Institute of Urban*
9 *Environment, Chinese Academy of Sciences, Xiamen, 361021, China,*

10 *⁴Shenzhen Key Laboratory of Organic Pollution Prevention and Control, School of*
11 *Eco-Environment, Harbin Institute of Technology Shenzhen, Shenzhen, 518055, China,*

12 *⁵School of Ocean and Geographic Science, Yancheng Teachers University, Yancheng*
13 *224051, China,*

14 *⁶School of Natural Sciences, Centre for Climate & Air Pollution Studies, Ryan Institute,*
15 *University of Galway, University Road, Galway, Ireland,*

16 *⁷State Key Laboratory of Atmospheric Boundary Layer Physics and Atmospheric*
17 *Chemistry, Institute of Atmospheric Physics, Chinese Academy of Sciences, Beijing*
18 *100029, China.*

19 Corresponding author: Ru-Jin Huang, rujin.huang@ieecas.cn; Fang Zhang,
20 zhangfang2021@hit.edu.cn

21

22

23

24

25 **Abstract**

26 Simplified assumptions of aerosol mixing states in modeling often introduce
27 substantial uncertainties in estimating cloud condensation nuclei (CCN) concentrations
28 (N_{CCN}) and their climatic impacts. This study systematically investigates the contrasting
29 relationships between mixing states and CCN activity by combining field
30 measurements of hygroscopicity with the algorithm of entropy at two inland and coastal
31 sites. We show distinct seasonal variations of mixing state. In winter, externally-mixed
32 particles dominated both sites, with comparable mixing state indices (χ) of 0.38 ± 0.12
33 and 0.39 ± 0.09 respectively for coastal and inland air. However, measurements in
34 summer showed pronounced differences: aerosols in the coastal atmosphere exhibited
35 a higher degree of internal mixing ($\chi=0.69\pm 0.19$), whereas inland χ values only
36 increased moderately to 0.47 ± 0.12 . Aerosol mixing state is largely influenced by
37 primary emissions and secondary formation process. Externally-mixed particles
38 originate chiefly from anthropogenic emissions in inland or sea salt in coastal. With the
39 aging process, particles become more internally-mixed as the enhanced fraction of
40 more-hygroscopic mode. Both environments show the negative correlations between
41 the critical diameter (D_{cri}) and χ but with distinct decrement rates for coastal vs. inland
42 aerosols. Specially, D_{cri} exhibits heightened sensitivity to fluctuations in χ when $\chi < 0.5$.
43 This offers a practical approach to estimate D_{cri} from χ when the particles are not highly
44 aged. Further analysis reveals that N_{CCN} exhibits heightened sensitivity to fluctuations
45 in χ at low values. These results underscore that mixing states exert different control

46 over N_{CCN} in diverse environments and provide critical constraints for parameterizing
47 fine aerosols CCN activity in models.

48 **1. Introduction**

49 Atmospheric cloud condensation nuclei (CCNs) are complex mixtures of organic
50 and inorganic components. Their chemical and physical properties make quantifying
51 aerosol-cloud interactions challenging (Liu et al., 2018; Rosenfeld et al., 2019; Xu et
52 al., 2022, 2024; Virtanen et al., 2025), introducing uncertainties into climate effect
53 assessments (Charlson et al., 1992; Shrivastava et al., 2017; IPCC, 2021; Chen et al.,
54 2022a; Manavi et al., 2025). Accurate climate model predictions of aerosol impacts
55 require understanding aerosol mixing states under different atmospheric conditions and
56 their effects on CCN activity (Ching et al., 2016; Zheng et al., 2021a). Current models
57 often oversimplify mixing states by assuming pure internal or external mixing (Winkler,
58 1973; Stevens et al., 2019; Riemer et al., 2019; Zheng et al., 2021b). This is problematic
59 because mixing states directly determine particle hygroscopicity distribution and CCN
60 estimates (Wang et al., 2010; Tao et al., 2024). For example, internal-mixed aerosol
61 particles have unimodal hygroscopicity distribution, while the external-mixed particles
62 are characterized by the bimodal/trimodal or partly overlapping structures (Spitieri et
63 al., 2023; Liu et al., 2025). Such simplifications can lead to significant errors, e.g.,
64 Sotiropoulou et al. (2007) found that mixing state assumptions caused two-fold N_{CCN}
65 estimation errors in global models.

66 Systematic observations across diverse environments are critical because aerosol
67 mixing states exhibit pronounced spatial-temporal variations (Ye et al., 2018; Hughes

68 et al., 2018; Liu et al., 2025). For example, continental and coastal regions present
69 contrasting scenarios (Ramachandran et al., 2016). The continental areas are dominated
70 by anthropogenic emissions, where aerosol aging is driven by industrial and traffic-
71 related pollutants (Huang et al., 2014; Ren et al., 2023). Particles here undergo
72 progressive internal mixing via photochemical process and heterogenous reactions,
73 altering their hygroscopic properties (Ervens et al., 2010; Tao et al., 2021). While the
74 coastal regions feature dynamic interactions between marine aerosols (e.g., sea salt) and
75 continental pollutants (Schill et al., 2015; Collins et al., 2013; Cheung et al., 2020).
76 Seasonal shifts in air mass sources (e.g., marine vs. continental dominance) might
77 create unique mixing state patterns (Xu et al., 2020, 2021a). For instance, summer
78 photochemical aging and heterogenous processes in coastal areas can enhance the
79 degree of internal mixing, while winter often retains more external mixing due to the
80 presence of the sea-salt particles with less-hygroscopic organic matter.

81 The continental aerosols influence regional cloud formation, while coastal
82 aerosols may provide insights into the characteristics of marine aerosols in region. The
83 properties of marine aerosols are significantly different from those of continental
84 aerosols, and therefore have distinct climate feedback mechanisms (Bellouin et al.,
85 2020; Xu et al., 2024; Liu et al., 2024). However, the current models lack regional-
86 specific mixing state parameters and usually assume uniform mixing in both
87 environments. This could lead to large uncertainties in predicting CCN concentrations,
88 highlighting the need for site-specific observations. For example, Ren et al. (2018)
89 found that the impact of aerosol mixing state on CCN activation characteristics ranged

90 from -34% to +16 % in urban atmosphere. Comparison between a fully internal mixture
91 assumption and using the mixing state index from the particle-resolved model, Ching
92 et al. (2017) found the obvious overestimation in CCN concentration. Especially in the
93 regions eg., Amazon Basin, Central Africa and Indonesia, the particles appeared to be
94 more external, errors in CCN concentration would increase up to 100% (Hughes et al.,
95 2018). A detailed exploration of mixing state on CCN concentration in global scale was
96 conducted by Zheng et al. (2021a), and the results showed that the mixing state varied
97 spatially with more externally mixed over the North Atlantic Ocean, off the coasts of
98 Southern Africa, and Australia. Thus, assuming particles with internally-mixed would
99 introduce errors in CCN concentration of 50-100%.

100 Therefore, for quantifying the aerosol mixing state in the ambient atmosphere,
101 we apply the algorithm of entropy proposed by Riemer and West (2013) to investigate
102 the aerosol heterogeneity. This index has been applied to quantify the mixing state more
103 reasonably both in field campaigns (Zhao et al., 2021; Yuan et al., 2023) and model
104 simulations (Ching et al., 2016; Zheng et al., 2021a). However, most studies focused
105 on quantifying the particle heterogeneity in composition (Ching et al., 2019; Fierce et
106 al., 2020; Zhao et al., 2021). Here we concentrated on evaluating the heterogeneity in
107 aerosol hygroscopicity for sub-micron particles, which directly related to CCN budget.
108 By refereeing to Yuan et al. 2023, the heterogeneity in hygroscopicity was investigated
109 by combining in-situ measurements of probability distribution function of the
110 hygroscopicity with the algorithm of entropy. Briefly, the mixing state index χ , is
111 devised based on the concept of information entropy concerning the distribution of

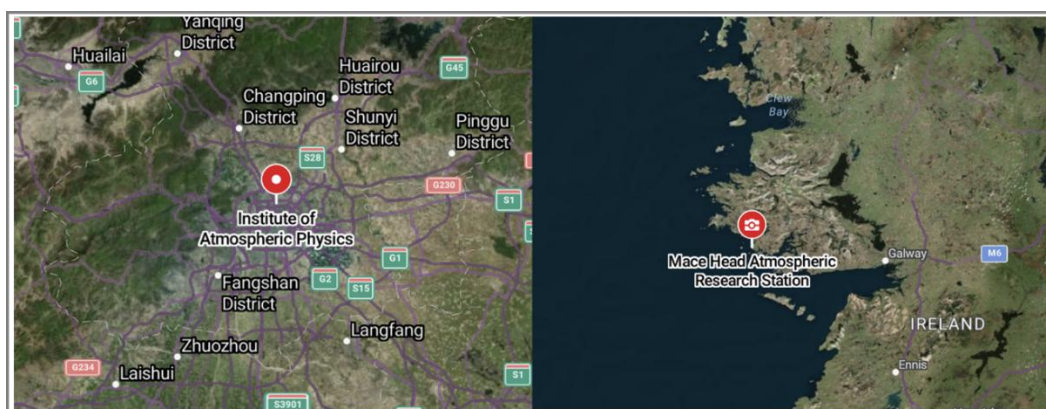
112 hygroscopicity across the aerosol population. It varies between 0 (external mixing
113 completely) and 1 (internal mixing completely). By integrating inland and coastal
114 measurements, this study will focus on addressing two key gaps, (1) How continental
115 vs. marine-dominated environments shape aerosol mixing states and CCN activity; (2)
116 Whether χ -based CCN parameterizations show regional dependencies, providing
117 critical constraints for climate models.

118 **2. Data and Methods**

119 **2.1 Field Campaigns**

120 The inland atmospheric measurements were conducted for two campaigns from
121 16 November to 6 December 2016 and 29 May to 13 June 2017 as a part of the Air
122 Pollution and Human Health (APHH) project (Shi et al., 2019), at the Institute of
123 Atmospheric Physics, Chinese Academy of Sciences (IAP, 39.97° N, 116.37° E) in
124 urban Beijing. The campaigns were complemented by the hygroscopicity and CCN
125 observations and were conducive to provide information on the aerosol hygroscopicity
126 affecting urban pollutions. This urban site exhibited highly variable aerosol populations
127 dominated by local anthropogenic sources including vehicular, cooking emissions, and
128 residential heating. Coastal measurements were performed at the Mace Head
129 atmospheric research station (MHD, 53.33° N, 9.90° W) from 1 November 2009 to 30
130 January 2010, and summer periods from 11 to 31 August 2009 and July 2010, which
131 located on the west coast of Ireland. Aerosol particles here experience alternating
132 influences from polluted continental and clean marine atmospheres. The map of the

133 sites was shown in Figure 1. More details about the campaigns were given in Fan et al.
134 (2020) and Xu et al. (2021a).



135
136 **Fig 1.** Map of the sites in the Inland of the Institute of Atmospheric Physics (IAP) and
137 Coastal of Mace Head (MHD). (© Google Maps, <https://maps.google.com/>, last access:
138 2 April 2025).

139 2.2 Instrumentation

140 Hygroscopicity measurements

141 The particle hygroscopicity at both sites was characterized using the humidified
142 tandem differential mobility analyzer (HTDMA). The hygroscopic growth factor (Gf),
143 defined as the ratio of the particle diameter at the fixed RH (90%) and dry diameter set
144 in this study for 40, 80, 110, 150, 200 nm at IAP and 35, 50, 75, 110 and 165 nm at
145 MHD, respectively. The RH calibration with ammonium sulfate for HTDMA system
146 was given in Fig. S1. The Gf probability density function (Gf-PDF) was derived using
147 the TDMAinv algorithm (Gysel et al., 2009). The number fraction (NF) of near-
148 hydrophobic mode (NH: $Gf \leq 1.21$), and more hygroscopic mode (MH: $Gf > 1.21$) in
149 IAP site was referred from Chen et al. (2022b). It was integrated into three modes for

150 the MHD site with the near-hydrophobic mode (NH: $1 < Gf < 1.3$), more hygroscopic
 151 mode (MH: $1.3 \leq Gf < 1.85$) and sea salt mode (SS: $Gf \geq 1.85$) for further examination
 152 (Xu et al., 2021a).

153 Here for each particle size, the hygroscopicity parameter κ can be subsequently
 154 calculated using κ -Köhler theory (Petters and Kreidenweis, 2007):

$$155 \quad \kappa = (Gf^3 - 1) \cdot \left[\frac{1}{RH} \exp\left(\frac{4\sigma_s M_w}{RT\rho_w D_d Gf}\right) - 1 \right] \quad (1)$$

156 where RH is the HTDMA relative humidity (90% set in the instrument), $\sigma_{s/a}$ is the
 157 surface tension of pure water (0.072 J m^{-2}), M_w and ρ_w are the molecular weight and the
 158 density of pure water, R is the gas constant, and T is the absolute temperature, D_d is the
 159 droplet diameter.

160 Then, the κ -PDF is obtained and normalized as $\int_0^\infty c(\kappa)d\kappa = 1$, where $c(\kappa)$ is
 161 normalized as κ -PDF. Further it was used to calculate the particle population
 162 heterogeneity (Calculation seen in Section 2.3).

163 According to the κ -Köhler theory, the critical diameter (D_{cri}) corresponding to the
 164 supersaturation ratio can be expressed as:

$$165 \quad D_{cri} = \sqrt[3]{\frac{4A^3}{27\kappa \ln^2 S}}, \quad A = \frac{4\sigma_s M_w}{RT\rho_w} \quad (2)$$

166 where S is the given supersaturation ratio (here 0.2% used in this study), κ is the mean
 167 value of the hygroscopicity parameter calculated in Equation (1).

168 **Chemical components**

169 For the inland atmospheric measurements, the non-refractory submicron aerosol
 170 (smaller than $1\mu\text{m}$, NR-PM₁) chemical composition was quantitatively characterized
 171 using the Aerodyne High-Resolution Time-of-Flight Aerosol Mass Spectrometer (HR-

172 ToF-AMS) (DeCarlo et al., 2006), including sulfate (SO_4^{2-}), nitrate (NO_3^-), ammonium
173 (NH_4^+), chloride (Chl) and organics (Org). The black carbon (BC) mass concentration
174 was determined from the light absorption with a seven-wavelength aethalometer (AE33,
175 Magee Scientific Corp.).

176 Measurements of PM_{10} in the coastal atmosphere were also performed by the HR-
177 ToF-AMS, including major inorganic salts (non-sea-salt sulfate, nss-SO_4^{2-} ;
178 methanesulfonic acid, MSA; NO_3^- ; NH_4^+) and organic matter. The sea salt was
179 quantified using NaCl ion signal, which has been demonstrated in previous studies
180 (Ovadnevaite et al., 2014). The instrument operation and calibration have been
181 described in previous studies (Ovadnevaite et al., 2014; Xu et al., 2019).

182 **Aerosol number size distribution and CCN number concentration**

183 Particle number size distributions (PNSD) were measured using an integrated
184 system consisting of a Differential Mobility Analyzer (DMA; model 3081, TSI Inc.)
185 coupled with a Condensation Particle Counter (CPC; model 3772, TSI Inc.). During the
186 measurements at IAP, the PNSD covered the size range of 10-550 nm with a 5-minute
187 time resolution. It scanned size range of 20-500 nm at MHD with a 10-minute temporal
188 resolution. The CCN number concentrations were quantified at both sites using a
189 Droplet Measurement Technologies CCN counter (DMT-CCNc) (Lance et al., 2006).
190 The instrument's supersaturation (SS) settings were carefully calibrated before and after
191 each campaign using ammonium sulfate aerosol following Rose et al. (2008) (Fig. S1).
192 Four effective supersaturations (SS) were 0.14%, 0.23%, 0.40% and 0.76% at IAP site.
193 Four SS levels were 0.25%, 0.5%, 0.75% and 1% at MHD site with an uncertainty of

194 $\pm 0.03\%$. Using measurements at set supersaturation of 0.2% as an example explores the
195 CCN activity in the following discussions.

196 **2.3 Calculation the heterogeneity for aerosol particles**

197 To characterize the heterogeneous distribution of the hygroscopic and non-
198 hygroscopic components in populations (Chen et al., 2022b), we calculated the mixing
199 state index (χ) using the κ -PDF, following the methodology of Yuan et al. (2023). Two
200 surrogate groups in a population of N aerosol particles were assumed (Zheng et al.,
201 2021a). One surrogate group consists the non- and/or slightly hygroscopic species with
202 κ_N of < 0.05 and another group contains the more hygroscopic species with κ_H of 0.5-
203 0.6 (Yuan et al., 2023, referred inorganics). Ambient particles typically contain one or
204 two of the components and the κ lies between 0 and 0.6 at IAP or 0.8 at MHD as shown
205 in Figure S2. Taking into account the enhanced hydrophilicity of marine aerosols at
206 MHD site, calculation assuming κ_H values of 0.7 and 0.8 were shown in Fig.
207 S3. While these variations in κ_H introduced a mean uncertainty of 8% in χ values, it
208 did not significantly affect the seasonal or site comparisons. The volume fraction of two
209 surrogate groups can be calculated based on the total κ according to the Zdanovskii–
210 Stokes–Robinson (ZSR) mixing rule (Zdanovskii, 1948; Stokes et al., 1966).

211 The mixing state index χ is defined as the affine ratio of the average particle
212 species diversity ($D\alpha$) and population species diversity ($D\gamma$) as:

$$213 \chi = \frac{D\alpha - 1}{D\gamma - 1} \quad (3)$$

214 The average per-particle species diversity $D\alpha$ can be calculated as follows. First,

215 the mixing entropies at bin i (H_i) are determined according to equation (4),

$$216 \quad H_i = -P_{i,N} \times \ln P_{i,N} - P_{i,H} \times \ln P_{i,H} \quad (4)$$

217 where $P_{i,N}$ and $P_{i,H}$ are the volume fraction of each group for the κ -PDF with X bins at
 218 bin i ($i=1,2,\dots,X$), and can be determined from the $P_{i,N} + P_{i,H} = 1$ and $P_{i,N} \times \kappa_N +$
 219 $P_{i,H} \times \kappa_H = \kappa_i$. Here $\kappa_N = 0.01, \kappa_H = 0.6$; κ_i represents the hygroscopicity parameter
 220 at bin i .

221 Based on the assumption that particles in the same diameter have the same mixing
 222 entropy $H_\alpha = \sum_{j=1}^N P_j \times H_j$, $P_j = \frac{V_j}{V_{total}} = \frac{1}{N}$; the per-particle mixing entropies H_α is
 223 determined according to equation (5),

$$224 \quad H_\alpha = \sum_{i=1}^X H_i \times c(\kappa)_i \times \Delta\kappa \quad (5)$$

225 where $c(\kappa)_i$ is the probability density of the normalized κ -PDF at bin i , and $\Delta\kappa$
 226 represents the bin width. Then, the average per-particle species diversity D_α can be
 227 determined as $D_\alpha = e^{H_\alpha}$;

228 The bulk population species diversity D_γ can be calculated as follows. First, the
 229 aerosol population of the mixing entropy can be calculated as equation (6):

$$230 \quad H_\gamma = -P_N \times \ln P_N - P_H \times \ln P_H \quad (6)$$

231 where P_N and P_H are the volume fraction of the non-hygroscopic and hygroscopic
 232 components in the population, and can be calculated by equation (7) and (8):

$$233 \quad P_N = \sum_{i=1}^X P_{i,N} \times c(\kappa)_i \times \Delta\kappa \quad (7)$$

$$234 \quad P_H = \sum_{i=1}^X P_{i,H} \times c(\kappa)_i \times \Delta\kappa \quad (8)$$

235 Then, the bulk population species diversity D_γ can be determined as $D_\gamma = e^{H_\gamma}$.

236 Here, the definition of surrogate species as supersets encompassing hygroscopicity

237 heterogeneity implies that the heterogeneity parameter χ ranges from 0 to 1. When the
238 mixing index χ approaches 0, it indicates a completely segregated state where
239 hygroscopic and non-hygroscopic species reside in distinct particles. For the case where
240 the mixing index χ is 1, it represents a homogeneous distribution of non-hygroscopic
241 and hygroscopic species throughout the aerosol population.

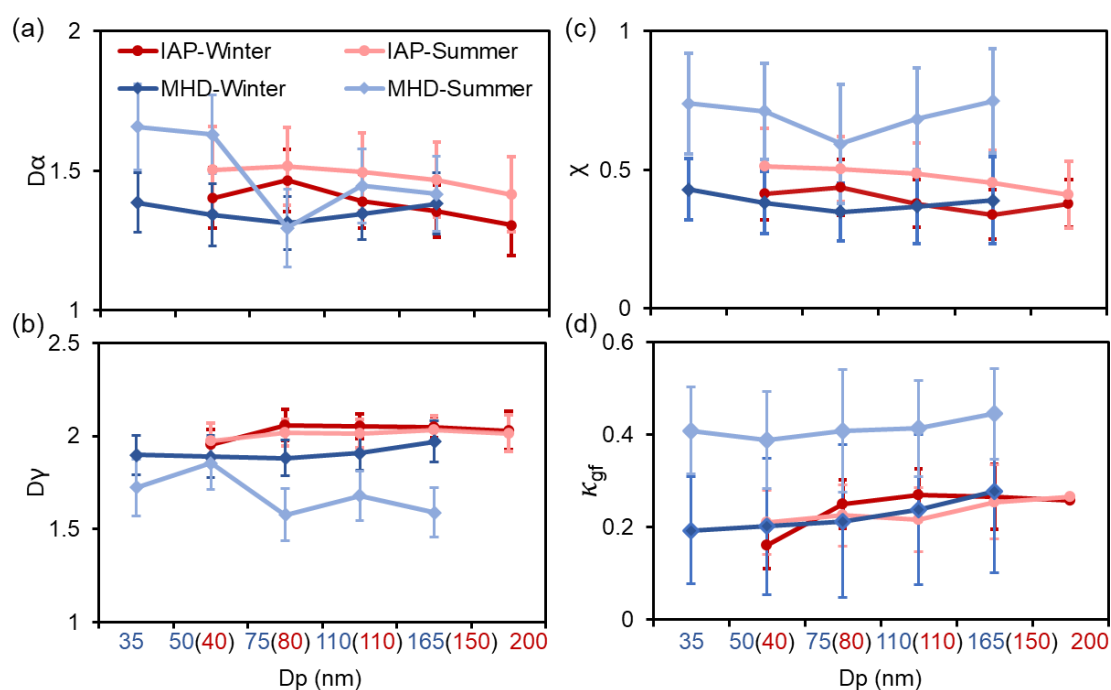
242 **3. Result and Discussion**

243 **3.1 Comparison of the heterogeneity in the inland and coastal atmosphere**

244 To characterize the hygroscopic heterogeneity of atmospheric aerosols, Figure 2
245 depicts variations in mixing state metrics ($D\alpha$, $D\gamma$, χ) and the hygroscopic parameter
246 (κ_{gf}) across particle size distributions. The $D\alpha$ and χ decrease with increasing particle
247 diameter, accompanied by higher κ_{gf} values at IAP site. This trend indicates that inland
248 particle populations tend to homogenize into hygroscopic compositions through
249 primary particle aging or secondary formation processes (Liu et al., 2025; Chen et al.,
250 2022b; Zhong et al., 2022). In contrast, particles exhibit a non-monotonic pattern at
251 MHD site: $D\alpha$ and χ decrease for Aitken-mode particles (<100 nm) but increase for
252 accumulation-mode particles. The κ_{gf} shows consistent size-dependent increases in
253 both winter and summer campaigns.

254 Notably, the mixing state metrics exhibit a pronounced minimum at 75 nm
255 particles, influenced by distinct mechanisms: winter minima reflect the high sea salt
256 fraction, while summer minima are driven by anthropogenic organic matter (Cheung et
257 al., 2020; Xu et al., 2021a). Lower winter χ values—coupled with broader κ -PDF

258 distributions—indicate stronger external mixing and compositional diversity compared
 259 to summer (Fig. S2). Seasonal χ and κ_{gf} disparities are more pronounced at MHD site,
 260 primarily driven by the seasonal alternation of marine and anthropogenic emission
 261 sources.



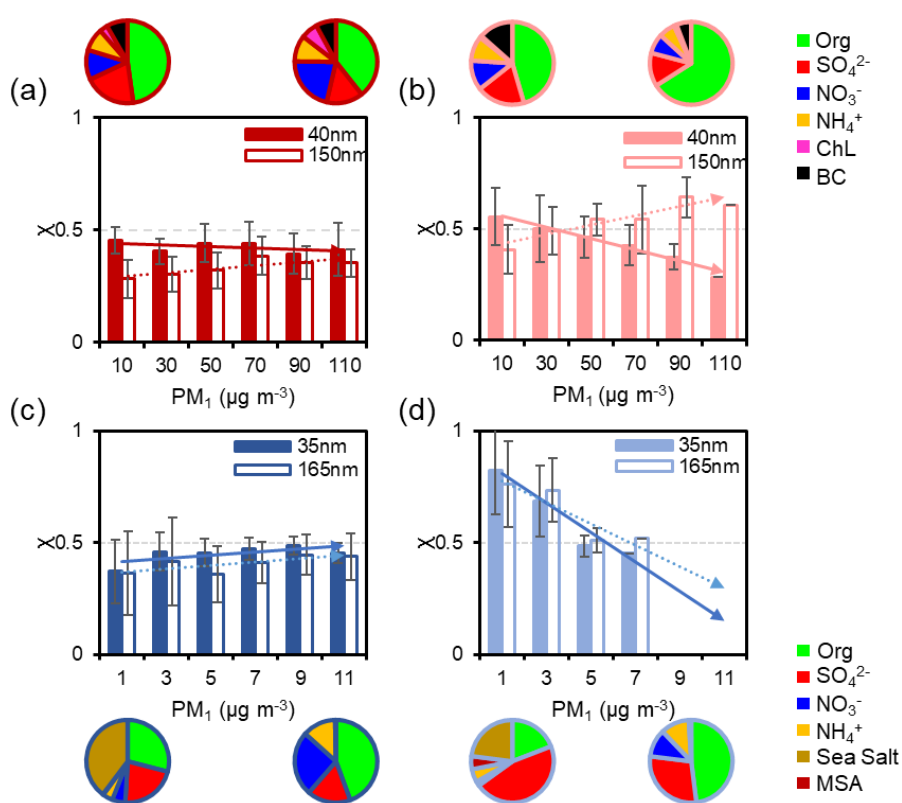
262
 263 **Fig 2.** Mean values of the $D\alpha$ (a), $D\gamma$ (b), χ (c) and κ_{gf} (d) for aerosols of five diameters
 264 during winter and summer periods at IAP and MHD sites.

265 Ultrafine particles (40 nm in IAP vs. 35 nm in MHD, Aitken mode) and larger
 266 particles (150 nm in IAP vs. 165 nm in MHD, accumulation mode) are selected to
 267 investigate distinct evolutionary processes of aerosol heterogeneity (Fig. 3 and Fig. S4).
 268 With the increasing of PM_{10} concentration during winter, the variation in χ values exhibit
 269 only minor both at the IAP and MHD sites, generally fluctuating between
 270 approximately -0.04 and 0.08 (Fig. 3a and c). Inland accumulation-mode particles
 271 show a modest increase in χ , corresponding with a higher proportion of inorganic salts.

272 Conversely, at MHD site, the composition fraction shifts from a sea-salt dominance
273 toward organic matter, accompanied by a ~20 % increase in nitrate content (Fig. 3c). In
274 summer, the variation of χ with PM concentration becomes markedly pronounced at
275 both IAP and MHD stations. For example, χ for 40 nm particles decreases as PM
276 increases at IAP site (Fig. 3b). The elevated particle heterogeneity mainly arises from
277 the locally primary emissions, corresponding to the enhanced primary organic
278 emissions as shown in Fig. S5. It appeared more pronounced during evening rush hours.
279 In contrast, χ for 150 nm particles increases from ~0.40 to ~0.60 with rising PM,
280 reflecting enhanced secondary formation and internal mixing during pollution process
281 that render the particle population more homogeneous. At coastal sites, χ declines with
282 rising PM by approximately 0.37 for 35 nm particles and 0.24 for 165 nm particles,
283 mirroring the shift in chemical composition makeup from inorganic dominance to
284 greater organic content (Fig. 3d).

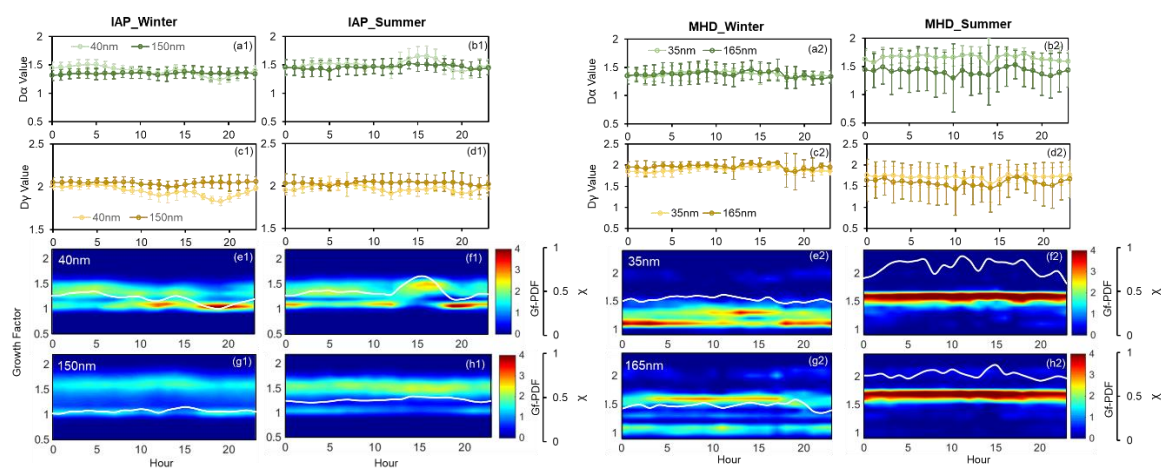
285 Diurnal variations of mixing state metrics ($D\alpha$, $D\gamma$, Gf-PDF and χ) at IAP and
286 MHD sites are shown in Figure 4. In IAP-winter, particles exhibited steeper declines in
287 $D\alpha$ and χ during evening rush hours than summer, indicating a higher fraction of non-
288 hygroscopic particles (40 nm) from fresh traffic emissions (Fig. 4a1 and S5).
289 Concurrently, reduced $D\gamma$ values suggest that the bulk population consists of uniformly
290 distributed less-hygroscopic (LH) components (Fig. 4c1). Aitken mode particles
291 showed bimodal and broader Gf-PDF distributions, corresponding to cooking activities
292 (11:00–13:00 LT) and traffic peaks (17:00–20:00 LT) (Cai et al., 2020). Midday
293 photochemical aging promoted more internally mixed aerosols (Yang et al., 2012; Liu

294 et al., 2025), as evidenced by increasing $D\alpha$ at the urban site (Fig. 4b1). Conversely, the
 295 χ for accumulation-mode particles showed minimal diurnal variations both in IAP-
 296 winter and IAP-summer. This is mainly due to the dominant hygroscopic mode for 150
 297 nm particles (Fig. 4g1 and 4h1), especially during summer, which is mainly from
 298 secondary formation or aging of the primary particles (such as the transformation from
 299 primary organic aerosol (POA) to secondary organic aerosol (SOA) in Fig. S5) (Wang
 300 et al., 2019; Fan et al., 2020).



301
 302 **Fig 3.** Variation of the average χ for 40 nm and 150 nm particles at IAP and 35 nm and
 303 165 nm at MHD site with the particle mass concentration in IAP-winter (a), IAP-
 304 summer (b), MHD-winter (c) and MHD-summer (d). The pie charts represent the
 305 average mass fraction during four field measurements.

306 For the coastal atmosphere, the mixing state metrics ($D\alpha$, $D\gamma$, and χ) of Aitken and
 307 accumulation mode particles in winter exhibited analogous diurnal patterns,
 308 characterized by a descending trend at nightfall (Fig. 4a2-h2). This corresponds to an
 309 enhanced modal distribution of near-hydrophobic (NH) particles at 35 nm and more-
 310 hygroscopic (MH) particles at 165 nm. In summer, $D\alpha$ and $D\gamma$ both trended downward
 311 during daytime, with the decline of $D\gamma$ being more pronounced. A conspicuous seasonal
 312 discrepancy between Aitken and accumulation mode particles was observed in this
 313 region (Fig. 4a2-h2), where the mixing state index χ increased incrementally from
 314 winter to summer. Specifically, the mean χ for 35 nm particles escalated from 0.42 to
 315 0.80, and for 165 nm particles, it rose from 0.39 to 0.76. This trend demonstrates a
 316 strong alignment with the spread factor (used as a measure of particle mixing state)
 317 documented by Xu et al. (2021a).



318
 319 **Fig 4.** Diurnal variation of $D\alpha$, $D\gamma$, Gf-PDF, and χ during winter and summer periods
 320 for 40 nm and 150 nm aerosols at IAP (a1-h1) and for 35 nm and 165 nm aerosols MHD
 321 site (a2-h2).

322 Similar to the mixing state χ , a very clear seasonal pattern of the aerosol
323 hygroscopic distribution was found (Fig. 4e-h). In winter, the Gf-PDF diurnal profiles
324 of both Aitken and accumulation mode particles showed bimodal distribution (Fig. 4e2-
325 g2) as evident by the number fraction of nearly-hydrophobic and more hygroscopic
326 modes (Fig. S6). The NH mode is likely composed of anthropogenic organic matter and
327 biogenic species derived from marine air masses (Xu et al., 2020), with this
328 composition being particularly prominent in the Aitken mode. Additionally, Xu et al.
329 (2021a) observed a higher abundance of the NH-mode in marine polar and Arctic air
330 masses, this further supports the notion that NH particles are likely of biogenic origin,
331 aside from contributions from anthropogenic activities. The more hygroscopic and sea
332 salt mode was mostly contributed from the nss-sulfate and sea salt in winter (Xu et al.,
333 2021a). Analogously, accumulation mode particles with a higher proportion of MH and
334 SS mode (Fig. S6) primarily attributed to the prevalence of non-sea-salt sulfate (nss-
335 sulfate) and sea salt in the coastal atmosphere (Xu et al., 2020). The bimodal and broad
336 of hygroscopic distribution suggested that particles were more diverse and external
337 mixed, consistent with the lower χ value in winter.

338 In contrast, summer observations revealed that Gf-PDFs of both Aitken and
339 accumulation mode particles transitioned to unimodal distributions, signifying particles
340 in summer had more homogeneous composition with a large extent of internal mixing
341 particles (with higher χ). Such diurnal trend in Gf-PDFs was consistent along with the
342 high number fraction of MH-mode and low NH-mode (Fig. S6). The higher
343 hygroscopicity and MH mode in summer were largely driven by the enhancement of

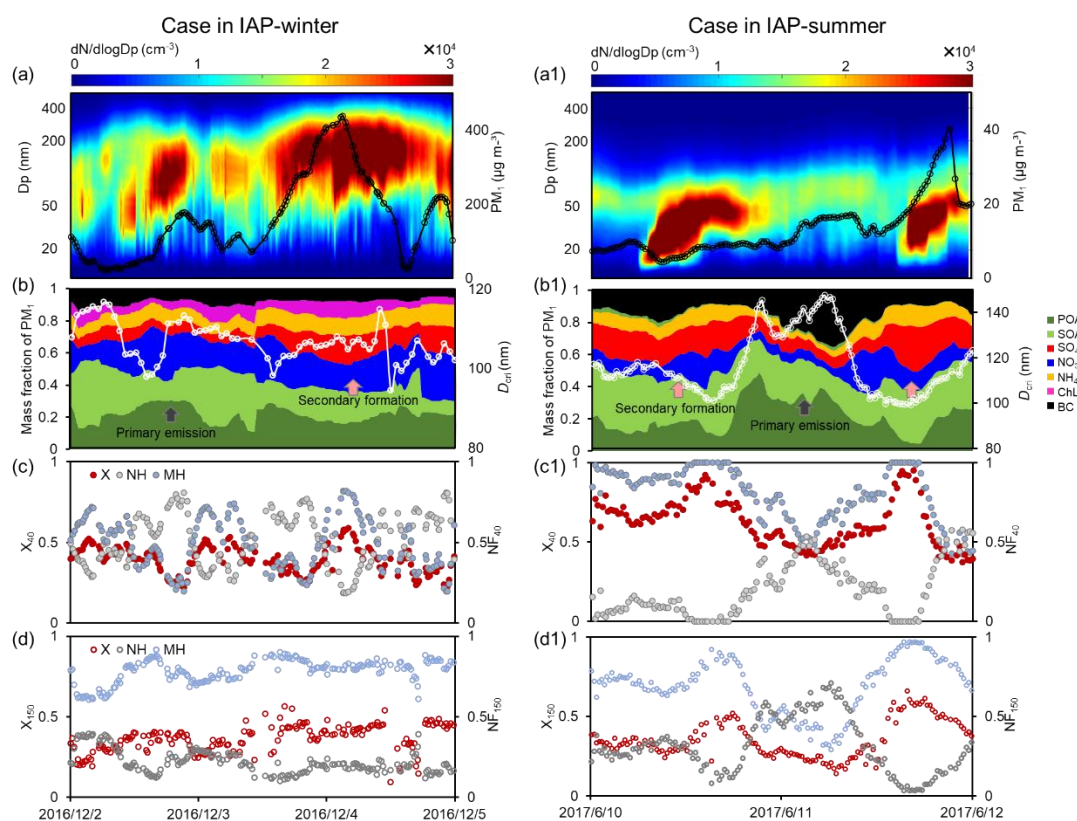
344 sulfate and decrease of organic matter (Fig. S6). And a clear shift from NH to MH mode
345 at midday might further demonstrate the promotion of photochemical aging in summer
346 (Xu et al., 2021a).

347 **3.2 Impacts of Primary Aerosol Emissions and Secondary Aerosol Formation on** 348 **Aerosol Mixing State**

349 As already noted above, changes in χ were clearly associated with the chemical
350 composition varying with site and season. The relationships between the mixing state
351 index and the number fraction of hydrophobic and hygroscopic mode during four
352 campaigns are presented in Figure S7. The χ exhibited negative correlations with the
353 fraction of hydrophobic mode but a positive relationship with the fraction of
354 hygroscopic particles, highlighting the markedly different effects of the primary
355 emissions and secondary formation on aerosol mixing state (Tao et al., 2024). To gain
356 more insight on this effect between inland and coastal atmosphere, four case are
357 analyzed (Fig. 5 and 6): case for IAP-winter, case for IAP-summer, case for MHD-
358 winter and case for MHD-summer.

359 Case for IAP-winter is a heavy polluted event with the mean PM mass
360 concentration increased from 22 to 437 $\mu\text{g m}^{-3}$ (Fig. 5a-d). The 40- and 150-nm χ
361 patterns shifted quickly during the pollution periods. With the mass fraction of
362 hydrophobic compounds (ie., POA) in PM_{10} increased, the χ of 40-nm particles
363 decreased from 0.5 to 0.2, that is, an enhanced NH mode and a weaken MH mode (Fig.
364 5b-c). At this stage, large particles for 150 nm are mainly from aqueous formation with
365 more proportion of nitrate. The corresponding χ of 150- nm particle was higher. While

366 with that the mass fractions of secondary organic and inorganic compositions increased,
 367 particles were more internal mixed with χ increased to be 0.6 for 40-nm and 0.53 for
 368 150-nm particles.

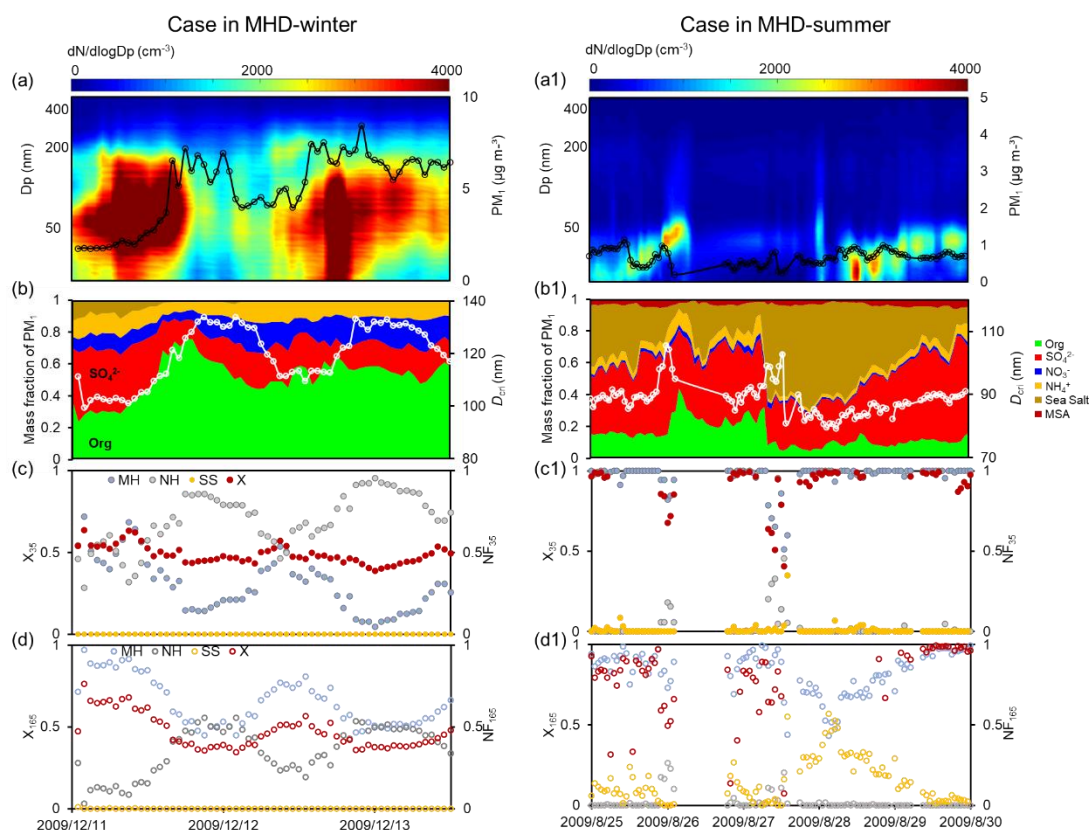


369

370 **Fig 5.** Case in IAP-winter (a-d) and IAP-summer (a1-d1). Particle number size
 371 distribution and PM_{10} (a and a1), mass fraction of the PM_{10} and the critical diameter (D_{cri})
 372 (b and b1), mixing state index (χ), number fraction of the nearly hydrophobic mode
 373 (NH) and more hygroscopic mode (MH) for 40 nm particles (c and c1), χ , NH and MH
 374 for 150 nm particles (d and d1).

375 Case for IAP-summer is the typical new particle formation events (NPF) with the
 376 mean PM_{10} of $13 \mu g m^{-3}$ (Fig. 5a1-d1). With the evolution of NPF events, the χ of 40-
 377 and 150-nm particles increased to be 0.95 and 0.61 with the enhanced proportion of

378 more-hygroscopic components (ie., SOA, NO₃⁻, SO₄²⁻). The χ pattern is opposite of that
 379 the number fraction of NH mode and consistent with the variation of MH mode (Fig.
 380 S7). Note that a sudden decrease in χ on June 11th was disturbed by the strong primary
 381 emission. The chemical mass fractions showed more POA and black carbon with an
 382 enhanced NH mode and a weaker MH mode (Fig. 5b1-d1). The χ of 40-nm particles
 383 decreased to be 0.4 and that of the 150-nm particles decreased to be 0.2. The χ patterns
 384 appear to similar transitions for Aitken and accumulation-mode particles during haze
 385 and NPF events. The increase in χ is synchronous with the increase in MH mode from
 386 secondary formation but opposite with that of LH mode from primary emissions. This
 387 implies that the primary emissions would lead particles more external mixing while
 388 secondary formation would promote aerosol more internal mixed in Inland atmosphere.



389

390 **Fig 6.** Case in MHD-winter (a-d) and MHD-summer (a1-d1). Particle number size

391 distribution and PM_{10} (a and a1), mass fraction of the PM_{10} and the critical diameter (D_{crit})
392 (b and b1), mixing state index (χ), number fraction of the nearly hydrophobic mode
393 (NH) and more hygroscopic mode (MH) for 35 nm particles (c and c1), χ , NH and MH
394 for 165 nm particles (d and d1).

395 Case for MHD-winter is a high organic matter pollution event with the mean PM_{10}
396 of $5.2 \mu\text{g m}^{-3}$ and 52% mass fraction of organics (Fig. 6a-d). Larger presence of
397 anthropogenic organic matter resulted the NH mode for 35-nm particles to be 95% and
398 165-nm particles to be 53% (Fig. 6). The χ of 35- and 165-nm particles decreased with
399 the NH mode increased (Fig. S7), similar with the case for IAP site. There was a steady
400 increase in χ when the MH-mode particles started increasing with the increase in mass
401 fraction inorganics, eg., 35 nm particles showed the mean χ increasing from 0.43 to
402 0.57 and 165 nm particles from 0.35 to 0.6. This indicated that the trend of aerosol
403 mixing state closely followed the evolution emission and secondary formation.

404 Case for MHD-summer is an extremely clean event with the mean PM_{10} of $0.7 \mu\text{g}$
405 m^{-3} (Fig. 6a1-d1). The dominated MH mode was found throughout the case, which
406 could be attributed from the high mass fraction of nss-sulfate (41% average). Compared
407 with the case in MHD-winter, the mean proportion of organic has decreased to be 15%.
408 Therefore, the χ remains at a high value (mean χ of 0.9 for 35-nm and 0.8 for 165-nm
409 particles). Until August 28th, a stronger increase in the mass fraction of sea salt and
410 accordingly SS mode in larger-size particles was observed. The χ decreased rapidly
411 with the decrease in MH mode and enhanced SS mode, especially for the accumulation
412 mode particles, suggesting the sea spray production makes particles more externally

413 mixed.

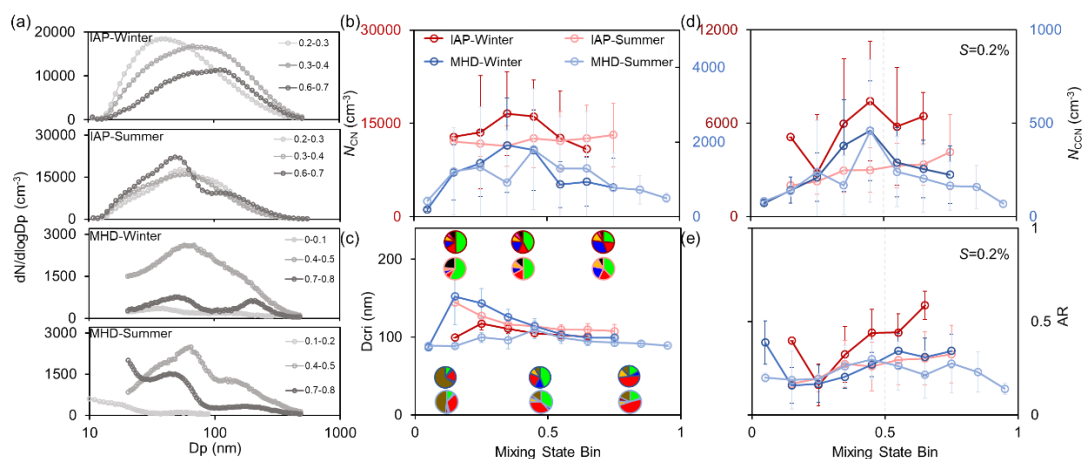
414 In summary, these results suggest that the primary emission and secondary
415 formation drive the hygroscopic distribution and can result in significant variation of
416 aerosol mixing state χ both in inland and coastal atmosphere. The pattern of χ varied
417 among site and season, highlighting the importance of considering the impact of mixing
418 state on CCN activity.

419 **3.3 Covariation relationships between the Mixing State and CCN Activity**

420 The mixing state of particle populations undergoes dynamic transformations
421 during atmospheric aging, profoundly influencing their CCN activity. Unlike prior
422 CCN closure studies that assumed mixing states based on chemical component
423 fractions (Yang et al., 2012; Padró et al., 2012; Ren et al., 2018), this work employs the
424 hygroscopicity distribution- and entropy-derived mixing state index χ to clarify the
425 covariation relationships between the mixing state and CCN activity. Given that CCN
426 activity reflects the characteristics of the entire particle population while χ is calculated
427 from HTDMA measurements at specific particle diameters, this study chooses the N_{CCN} ,
428 activation ratio (AR) at supersaturation of 0.2% and the mean χ for accumulation-mode
429 to illustrate the covariation characteristic approximately. This approach is employed to
430 ensure that both variables/parameters reflect the characteristics of the accumulation-
431 mode particle population. The covariations of particle size and chemical composition
432 with the mixing state (χ ranging from 0 to 1 at intervals of 0.1) are illustrated in Figure
433 7. This figure provides key insights into two fundamental determinants of CCN activity

434 (Dusek et al., 2006).

435 As χ increases, the peak diameter (D_{peak}) of the particle number size distribution
 436 (PNSD) shifts toward larger sizes (Fig. 7a and Fig. S8), while peak concentrations occur
 437 within the intermediate χ range (0.3–0.6). This trend indicates that CN number
 438 concentration (N_{CN}) first increases, driven by primary emissions and new particle
 439 formation, then decreases due to mixing and aging processes (Fig. 7b). Notably, new
 440 particle formation events frequently occurred in IAP-summer (Fig. S9), corresponding
 441 the gradually increase of χ . And the χ for Aitken-mode is significantly larger than the
 442 accumulation-mode particles during this period. Thus, N_{CN} exhibits a sustained slight
 443 increase as the degree of the internal mixing increases in IAP-summer.



444
 445 **Fig 7.** Comparison of the average particle number size distribution (PNSD) in different
 446 mixing state index (χ) (a), CN number concentration (N_{CN}) as a function of χ (b),
 447 Critical diameter (D_{cri}) at $S=0.2\%$ and mass fraction of chemical composition as a
 448 function of χ (c), CCN number concentration (N_{CCN}) (d) and activation ratio (AR) at
 449 $S=0.2\%$ a function of χ (e).

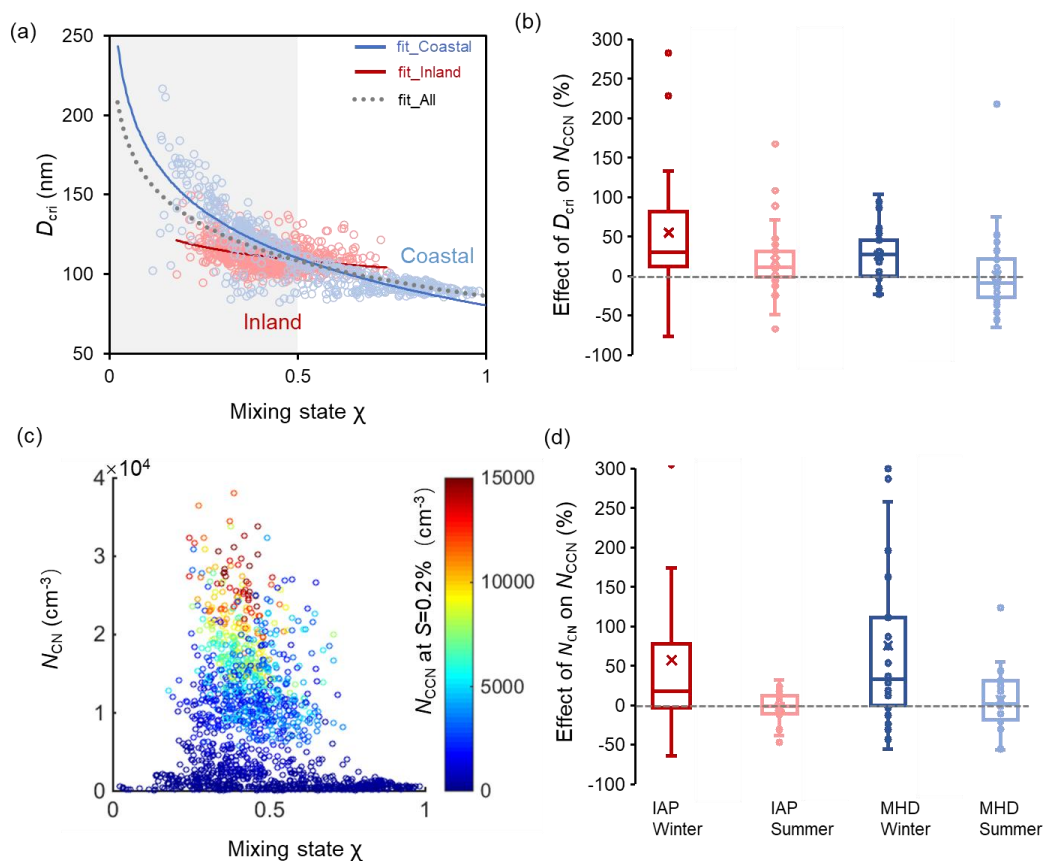
450 The critical diameter (D_{cri})—defined as the minimum size required for activation

451 at a given supersaturation—depends on aerosol hygroscopicity. In turn, this
452 hygroscopicity is jointly determined by the hygroscopicity of individual soluble
453 components and their mass fractions in the aerosol (Petters and Kreidenweis, 2007).
454 Using measurements at supersaturation of 0.2% as an example, Fig. 7c shows that D_{cri}
455 decreases with increasing highly hygroscopic inorganic components (e.g., sulfate,
456 nitrate) in the inland atmosphere. In contrast, coastal D_{cri} exhibits nonlinear variations
457 with χ : high external mixing (low χ) elevates D_{cri} due to dominant organic components,
458 reducing sea salt particle fractions. As χ increases, the mass fraction of non-sea-salt
459 sulfate (nss-sulfate) rises, enhancing activation potential by decreasing D_{cri} .

460 The covariation characteristic of CCN activity at 0.2% supersaturation with
461 mixing state index χ reveals distinct inter-atmospheric differences, as shown in Fig. 7d-
462 e. In IAP, N_{CCN} at $S=0.2\%$ demonstrates a monotonic increasing trend with χ , attributed
463 to the synergistic effects of rising N_{CN} and decreasing D_{cri} (Fig. S10). By contrast,
464 coastal N_{CCN} follows a pattern analogous to N_{CN} , with peak concentrations shifting
465 toward higher χ values. This highlights the dominant role of particle size effects in
466 enhancing CCN concentrations under marine-influenced conditions (Dusek et al.,
467 2006).

468 Two distinct $D_{\text{cri}}-\chi$ trends underpin these disparities: one remains stable, driven by
469 the inherent hygroscopicity of sea salt, while the other exhibits steep D_{cri} declines
470 associated with anthropogenic pollution as internal mixing intensifies. These
471 discrepancies are further manifested in the nonlinear $D_{\text{cri}}-\chi$ relationship. The activation
472 ratio (AR)—quantifying aerosol cloud droplet formation potential at fixed

473 supersaturation—also varies by site (Fig. 7e). Notably, AR shows a marked increase
 474 with χ in IAP-winter, likely due to enhanced N_{CCN} from the elevated inorganic fraction
 475 under higher mixing states (Fig. 3). Conversely, the inorganic fraction decreases during
 476 other sampling periods, dampening AR growth.



477
 478 **Fig 8.** Covariation characteristics of the critical diameter (D_{cri}) with the χ (a), relative
 479 change of CCN number concentration (N_{CCN}) at supersaturation $S=0.2\%$ with the
 480 reduction in D_{cri} (b); Covariation characteristics of the CN number concentration (N_{CN})
 481 with the χ , different colors represent the N_{CCN} (c), relative change of N_{CCN} with the
 482 change in N_{CN} (d).

483 The mixing state directly reflects the degree of particle aging, which subsequently
 484 influences the particle composition and size. Fig. 8 further examines the covariation

485 characteristics of CN concentration, chemical compositions (i.e., D_{cri}) with mixing state
486 across particle populations. The mixing state index quantifies the variance in
487 hygroscopic distribution that emerges directly from compositional heterogeneity. Thus,
488 it can indirectly affect D_{cri} by serving as an indicator of particle aging. The critical
489 diameter (D_{cri}) is intrinsically sensitive to the hygroscopic distribution—wherein
490 broader hygroscopic spectra (corresponding to lower χ) engender more extensive D_{cri}
491 ranges. As shown in Fig. 8a, the D_{cri} exhibits heightened sensitivity to minor χ
492 fluctuations in the mixing state (χ) when $\chi < 0.5$. This significant decrease in D_{cri} with
493 increasing χ further confirms the potential effect of aging degree on critical particle
494 diameter. In contrast, for particles already characterized by internal mixing, further
495 increases in χ (i.e., higher degrees of internal mixing) exert a negligible influence on
496 D_{cri} . Particularly when $\chi > 0.7$, the variation in D_{cri} with χ is within 20%. This behavior
497 pattern reflects the influence of hygroscopic heterogeneity on critical diameter and
498 might enable a novel parameterization for D_{cri} estimation. This behavior pattern implies
499 that the $D_{\text{cri}}-\chi$ relationship could enable a novel parameterization for D_{cri} estimation
500 when the aerosol particles are not highly aged or when the internal mixing degree of
501 aerosol particles is relatively low, serving as a novel framework for integrating mixing
502 state effects on CCN activity in atmospheric models.

503 Aerosol observation at MHD site (blue dots) span a broad D_{cri} range (80–220 nm)
504 with χ varying from 0.1 to 1, reflecting alternating influences of highly hygroscopic
505 inorganic salts (sea salt, sulfate) and less-hygroscopic organic matter. In contrast,
506 observation at IAP site that is dominated by anthropogenic aerosols exhibit a narrower

507 D_{cri} range (90–150 nm). Both environments show negative D_{cri} - χ correlations, but with
508 distinct functional forms. For instance, MHD aerosols feature an exceptional
509 logarithmic fit ($D_{\text{cri}} = -42.98\ln(\chi) + 80.36$, Pearson $r = -0.87$, $R^2 = 0.75$; Fig. 8a blue
510 line), while IAP aerosols (red line) yield a shallower slope (-12.04) and Pearson r of -
511 0.4. This quantifies that D_{cri} sensitivity to χ is 3.6 times steeper in MHD environments.
512 This behavior pattern implies that the D_{cri} - χ relationship could enable a novel
513 framework for D_{cri} estimation. The slope reflects the compositional diversity of the
514 regime, steeper slopes occur where small χ variations correspond to large compositional
515 shifts (e.g., sea salt in coastal site). As discussed above, strong impact of primary
516 emission and secondary formation on aerosol mixing state was observed in both sites
517 (Fig. 5 and 6). One could obtain more details on the D_{cri} - χ correlations. For example,
518 the D_{cri} exhibited rapidly increase with the increase of primary emissions (ie., mass
519 fraction of POA enhanced) during polluted periods. The D_{cri} pattern appeared opposite
520 with that of the mixing state index, especially for the accumulation-mode particles.
521 More pronounced D_{cri} - χ correlations were observed during the new particle formation
522 (Fig. 5a1-d1). The decreasing presence of D_{cri} matched the increasing proportion of
523 SO_4^{2-} and SOA with the χ increased during NPF events. Similar correlations between
524 the critical diameter and mixing state index were also found in the coastal atmosphere,
525 especially for the case of the enhanced anthropogenic organic matter and sea salt
526 production (Fig. 6). This implies that the relationship between the D_{cri} and χ might be
527 disturbed by the variation of emission pollution and secondary formation processes,
528 resulting in spatiotemporal differences. The D_{cri} reduces by 2.2–6.8% with the mixing

529 state increase at a step of 0.1, with the steepest winter decline (Fig. S11).

530 Changes in N_{CN} with differ starkly between environments: positive effects in polluted
531 inland air (+9%) versus negative effects in coastal regions (-2%). Aerosols in IAP,
532 frequently perturbed by primary emissions and new particle formation, exhibit elevated
533 N_{CN} (peaking at $\chi = 0.2\text{--}0.7$), while in MHD N_{CN} remains $\sim 5000 \text{ cm}^{-3}$ across all χ . We
534 categorized data into two groups: C1 (particles within specific N_{CN} ranges) evaluates
535 N_{CCN} covariations mainly driven by $D_{\text{cri}}\text{-}\chi$ relationships, while C2 (particles within fixed
536 D_{cri} intervals) assesses $N_{\text{CN}}\text{-}\chi$ effects (Fig. 8b). Relative changes (RC) in D_{cri} , N_{CN} , and
537 N_{CCN} with χ were calculated by comparing successive χ increments (χ^{i+1} vs. χ^i ,
538 $i=0,0.1\dots 1$) within defined N_{CN} or D_{cri} windows.

539 Notably, the covariation relationship between the N_{CCN} and mixing state exerts more
540 pronounced for the case of externally mixed aerosols dominated. For example, MHD-
541 winter aerosols (high external mixing; $\chi_{\text{mean}}=0.38\pm 0.12$) showed RCs in N_{CCN} of 23%
542 (C1) and 72% (C2), whereas MHD-summer aerosols (high internal mixing;
543 $\chi_{\text{mean}}=0.69\pm 0.19$) exhibited negligible effects (-2.5% in C1, 0.9% in C2). Inland
544 atmospheres, despite smaller seasonal χ variations, showed analogous trends: RCs of
545 N_{CCN} in winter (55% in C1, 57% in C2 for external mixing) exceeded summer values
546 for more internally mixed populations (Fig. 8d). These results confirm that hygroscopic
547 heterogeneity strongly influences N_{CCN} under external mixing, aligning with prior work
548 (Ching et al., 2017).

549 The covariation characteristics are most pronounced during winter in both
550 environments, attributed to heightened winter D_{cri} sensitivity to χ : a 0.1 χ increase

551 reduces D_{crit} by 5.2% (winter), boosting N_{CCN} by 39%, versus 2.4% D_{crit} reduction
552 (summer) yielding only 6% N_{CCN} enhancement. Concomitantly, winter $N_{\text{CN}}-\chi$ effects on
553 N_{CCN} reach 65%, far exceeding summer responses.

554 In contrast to previous evaluation methods that oversimplify mixing states (Ren et
555 al., 2018; Xu et al., 2021b), the entropy-based framework employed in this study
556 explicitly characterizes the covariation between the CCN activity and transitions in the
557 mixing state. Aerosols in IAP-winter are presumably shaped by intense urban pollution
558 sources—including traffic emissions, residential heating, and cooking activities—
559 thereby enriching the externally mixed particle fraction (Fan et al., 2020; Xie et al.,
560 2020). Analogously, aerosols in MHD-winter exhibit dominant external mixing,
561 consisting of near-hydrophobic and hydrophilic particle mixtures (Xu et al., 2021a). As
562 illustrated in Fig. S2, the winter aerosol population exhibits bimodal or multimodal κ -
563 PDF distributions—this pattern indicates a high degree of external mixing, with the
564 aerosols characterized by chemically diverse compositions. Collectively, these results
565 underscore the pivotal role of mixing state heterogeneity in modulating CCN activity
566 across different environments.

567 **4. Conclusions**

568 The mixing state of aerosol populations undergoes complex transformations
569 during atmospheric aging, altering the distribution of hygroscopic and non-hygroscopic
570 components and thus influencing CCN activity (Xu et al., 2021a; Ching et al., 2017).
571 This study derived a mixing state index (χ) from field-measured hygroscopicity
572 distributions, systematically investigating the covariation relationship between the

573 mixing state and CCN activity at two inland and coastal environments. Results provide
574 field evidence that aerosol mixing states generally reside between purely internal and
575 external extremes (Chen et al., 2022b). Aerosol mixing state is largely influenced by
576 the primary emissions and secondary formation process. Externally-mixed particles
577 with more hydrophobic-mode originate chiefly from primary emissions in IAP, while
578 those of more sea-salt mode from sea spray in MHD. While it becomes more internally-
579 mixed as the enhanced fraction of more-hygroscopic mode and decreased fraction of
580 hydrophobic mode during the aging process. This highlights a dual regulatory
581 mechanism of mixing state and its potential impact on hygroscopic distribution and
582 CCN activity.

583 As χ increases, CN number concentrations (N_{CN}) first rise—driven by primary
584 emissions and new particle formation—then decline due to condensation and
585 coagulation during aging. The critical diameter (D_{cri}) exhibits heightened sensitivity to
586 minor χ fluctuations when $\chi < 0.5$. In contrast, for particles already characterized by
587 internal mixing, further increases in χ (i.e., higher degrees of internal mixing) exert a
588 negligible influence on D_{cri} . Additionally, both environments show negative $D_{\text{cri}} - \chi$
589 correlations, but with distinct functional forms. We propose a practical approach for
590 estimating D_{cri} from χ , applicable when the aerosol particles are not highly aged or when
591 the internal mixing degree of aerosol particles is relatively low, serving as a novel
592 framework for integrating mixing state effects on CCN activity in atmospheric models.

593 Entropy-based analyses further support the covariation relationships between the
594 mixing state and N_{CCN} , especially for externally mixed aerosols. Current models often

595 oversimplify aerosol mixing states as purely internal or external (Stevens et al., 2019;
596 Bauer et al., 2013), the latter being particularly sensitive to organic matter (Ren et al.,
597 2018; Bhattu et al., 2015). Such simplifications introduce significant biases in N_{CCN}
598 estimation (Riemer et al., 2019; Ching et al., 2019). The χ - D_{cri} parameterization
599 proposed here offers a novel approach to reduce model complexity in representing
600 aerosol hygroscopicity and CCN activation, enabling more accurate simulations of
601 aerosol CCN capacity. It is expected mitigate the underestimation in CCN compared
602 with the complete external mixing assumption, while effectively alleviates the
603 overestimation that arises from applying the complete internal mixing assumption in
604 regions characterized by high external mixing (Zheng et al., 2021a). This advancement
605 improves our understanding of aerosol-cloud interactions (IPCC, 2021; Rosenfeld et al.,
606 2019), critical for refining climate effect assessments.

607 **Data availability**

608 All data used in the study are available at <https://doi.org/10.3974/geodb.2019.06.11.V1>
609 (Fan et al., 2019) and <http://doi.org/10.17632/3dx6pnx869.1> (Xu et al., 2021a).

610 **Author contributions**

611 RH and JR conceived the conceptual development of the paper. JR, FZ and WX directed
612 and performed the experiments with YW and LC. FZ and YS provided the dataset in
613 the inland site. JO, DC and CO provided the dataset in the coastal site. JR conducted
614 the data analysis and wrote the draft. All authors edited and commented on the various
615 sections of the paper.

616 **Competing interests**

617 The contact author has declared that none of the authors has any competing interests.

618 **Supporting Information**

619 Additional analysis results that were applied in this study. Example of calibration
620 results of HTDMA and CCN used in this study (Figure S1), mean values of the κ -PDF
621 for aerosols of five diameters (Figure S2), sensitivity of the hygroscopic parameter for
622 the group of the hygroscopic species on the mixing state index χ (Figure S3), time series
623 of the average per-particle species diversity $D\alpha$, the bulk population species diversity
624 $D\gamma$, and their affine ratio χ (Figure S4), diurnal trend of particle size, chemical mass
625 fraction and number fraction (NF) of hydrophobic and hygroscopic mode in IAP
626 (Figure S5) and in MHD (Figure S6), mixing state as a function of number fraction of
627 hydrophobic and hygroscopic mode (Figure S7), variation of the peak diameter (D_{peak})
628 with the mixing state index (Figure S8), particle number size distribution and mixing
629 state during new particle formation events (Figure S9), diurnal variation of χ and CN
630 concentration during winter and summer periods for 40 nm and 150 nm aerosols in
631 inland and for 35 nm and 165 nm aerosols in coastal site (Figure S10), relative change
632 of the critical diameter and CN concentration with the mixing state index χ (Figure S11)
633 (PDF).

634 **Acknowledgements**

635 This work was funded by the National Natural Science Foundation of China (NSFC)
636 under Grant No. 42525301, 42405118 and 42475112, the State Key Laboratory of

637 Loess Science, Institute of Earth Environment, Chinese Academy of Sciences
638 (SKLLQG2429), the Guangdong Natural Science Foundation (Grant No.
639 2024A1515011005), Shenzhen Science and Technology Program (Grant No.
640 KCXST20221021111404011, SYSPG20241211173609007). We thank all participants
641 of the field campaign for their hard work and sharing of the data.

642 **References**

- 643 Bhattu, D., Tripathi, S. N.: CCN closure study: Effects of aerosol chemical composition
644 and mixing state, *Journal of Geophysical Research: Atmospheres.*, 120(2), 766–
645 783, <https://doi.org/10.1002/2014JD021978>, 2015.
- 646 Bellouin, N., Quaas, J., Gryspeerdt, E., Kinne, S., Stier, P., Watson-Parris, D., Boucher,
647 O., Carslaw, K. S., Christensen, M., Daniau, A-L., Dufresne, J.-L., Feingold, G.,
648 Fiedler, S., Foster, P., Gettelman, A., Haywood, J. M., Lohmann, U., Malavelle, F.,
649 Mauritsen, T., McCoy, D. T., Schulz, M., Schwartz, S. E., Sourdeval, O.,
650 Storelvmo, T., Toll, V., Winker, D., and Stevens, B: Bounding global aerosol
651 radiative forcing of climate change, *Rev. Geophys.*, 58, e2019RG000660,
652 <https://doi.org/10.1029/2019RG000660>, 2020.
- 653 Bauer, S. E., Ault, A., Prather, K. A.: Evaluation of aerosol mixing state classes in the
654 GISS modelE-MATRIX climate model using single-particle mass spectrometry
655 measurements, *Journal of Geophysical Research: Atmospheres.*, 118, 9834–9844,
656 <https://doi.org/10.1002/jgrd.50700>, 2013.
- 657 Charlson, R. J., Schwartz, S. E., Hales, J. M., Cess, R. D., Coakley Jr, J. A., Hansen, J.
658 E., Hofmann, D. J.: Climate forcing by anthropogenic aerosols, *Science.*,
659 255(5043), 423–430, <https://doi.org/10.1126/science.255.5043.423>, 1992.
- 660 Chen, Y., Haywood, J., Wang, Y., Malavelle, F., Jordan, G., Partridge, D., Fieldsend, J.,
661 Leeuw, J. D., Schmidt, A., Cho, N., Oreopoulos, L., Platnick, S., Grosvenor, D.,
662 Field, P., Lohmann, U.: Machine learning reveals climate forcing from aerosols is
663 dominated by increased cloud cover, *Nature Geoscience.*, 15(8), 609–614,

664 <https://doi.org/10.1038/s41561-022-01027-9>, 2022a.

665 Chen, L., Zhang, F., Zhang, D., Wang, X., Song, W., Liu, J., Ren, J., Jiang, S., Li, X.,
666 and Li, Z.: Measurement report: Hygroscopic growth of ambient fine particles
667 measured at five sites in China, *Atmospheric Chemistry and Physics.*, 22, 6773–
668 6786, <https://doi.org/10.5194/acp-22-6773-2022>, 2022b.

669 Ching, J., Zaveri, R. A., Easter, R. C., Riemer, N., Fast, J. D.: A three-dimensional
670 sectional representation of aerosol mixing state for simulating optical properties
671 and cloud condensation nuclei, *Journal of Geophysical Research: Atmospheres.*,
672 121(10), 5912–5929, <https://doi.org/10.1002/2015JD024323>, 2016.

673 Ching, J., Fast, J., West, M., Riemer, N.: Metrics to quantify the importance of mixing
674 state for CCN activity, *Atmospheric Chemistry and Physics.*, 17(12), 7445–7458,
675 <https://doi.org/10.5194/acp-17-7445-2017>, 2017.

676 Ching, J., Adachi, K., Zaizen, Y., Igarashi, Y., Kajino, M.: Aerosol mixing state revealed
677 by transmission electron microscopy pertaining to cloud formation and human
678 airway deposition, *npj Climate and Atmospheric Science.*, 2(1), 22, [https://doi.org/](https://doi.org/10.1038/s41612-019-0081-9)
679 [10.1038/s41612-019-0081-9](https://doi.org/10.1038/s41612-019-0081-9), 2019.

680 Collins, D. B., Ault, A. P., Moffet, R. C., Ruppel, M. J., Cuadra-Rodriguez, L. A.,
681 Guasco, T. L., Corrigan, C. E., Pedler, B. E., Azam, F., Aluwihare, L. I., Bertram,
682 T. H., Roberts, G. C., Grassian, V. H., Prather, K. A.: Impact of marine
683 biogeochemistry on the chemical mixing state and cloud forming ability of nascent
684 sea spray aerosol, *Journal of Geophysical Research: Atmospheres.*, 118(15), 8553–
685 8565, <https://doi.org/10.1002/jgrd.50598>, 2013.

686 Cheung, H. C., Chou, C. C. K., Lee, C. S. L., Kuo, W. C., Chang, S. C.: Hygroscopic
687 properties and cloud condensation nuclei activity of atmospheric aerosols under
688 the influences of Asian continental outflow and new particle formation at a coastal
689 site in eastern Asia, *Atmospheric Chemistry and Physics.*, 20(10), 5911–5922,
690 <https://doi.org/10.5194/acp-20-5911-2020>, 2020.

691 Cai, J., Chu, B., Yao, L., Yan, C., Heikkinen, L. M., Zheng, F., Li, C., Fan, X., Zhang,
692 S., Yang, D., Wang, Y., Kokkonen, T. V., Chan, T., Zhou, Y., Dada, L., Liu, Y., He,

693 H., Paasonen, P., Kujansuu, J. T., Petäjä, T., Mohr, C., Kangasluoma, J., Bianchi,
694 F., Sun, Y., Croteau, P. L., Worsnop, D. R., Kerminen, V. M., Du, W., Kulmala, M.,
695 & Daellenbach, K. R.: Size-segregated particle number and mass concentrations
696 from different emission sources in urban Beijing, *Atmospheric Chemistry and*
697 *Physics.*, 20(21), 12721–12740, <https://doi.org/10.5194/acp-20-12721-2020>, 2020.

698 Dusek, U., Frank, G. P., Hildebrandt, L., Curtius, J., Schneider, J., Walter, S., Chand,
699 D., Drewnick, F., Hings, S., Jung, D., Borrmann, S., Andreae, M. O.: Size matters
700 more than chemistry for cloud-nucleating ability of aerosol particles, *Science.*, 312
701 (5778), 1375–1378, <https://doi.org/10.1126/science.1125261>, 2006.

702 DeCarlo, P. F., Kimmel, J. R., Trimborn, A., Northway, M. J., Jayne, J. T., Aiken, A. C.,
703 Gonin, M., Fuhrer, K., Horvath, T., Docherty, K. S., Worsnop, D. R., Jimenez, J.
704 L.: Field-deployable, high-resolution, time-of-flight aerosol mass spectrometer,
705 *Analytical Chemistry.*, 78, 8281–8289, <https://doi.org/10.1021/ac061249n>, 2006.

706 Ervens, B., Cubison, M. J., Andrews, E., Feingold, G., Ogren, J. A., Jimenez, J. L.,
707 Quinn, P. K., Bates, T. S., Wang, J., Zhang, Q., Coe, H., Flynn, M., Allan, J. D.:
708 CCN predictions using simplified assumptions of organic aerosol composition and
709 mixing state: a synthesis from six different locations, *Atmospheric Chemistry and*
710 *Physics.*, 10(10), 4795–4807, <https://doi.org/10.5194/acp-10-4795-2010>, 2010.

711 Fierce, L., Onasch, T. B., Cappa, C. D., Mazzoleni, C., China, S., Bhandari, J.,
712 Davidovits, P., Fischer, D. A., Helgestad, T., Lambe, A. T., et al.: Radiative
713 absorption enhancements by black carbon controlled by particle-to-particle
714 heterogeneity in composition, *P. Natl. Acad. Sci. USA*, 117, 5196–5203,
715 <https://doi.org/10.1073/pnas.1919723117>, 2020.

716 Fan, X., Liu, J., Zhang, F., Chen, L., Collins, D., Xu, W., Jin, X., Ren, J., Wang, Y., Wu,
717 H., Li, S., Sun, Y., Li, Z.: Contrasting size-resolved hygroscopicity of fine particles
718 derived by HTDMA and HR-ToF-AMS measurements between summer and
719 winter in Beijing: the impacts of aerosol aging and local emissions, *Atmospheric*
720 *Chemistry and Physics.*, 20(2), 915–929, <https://doi.org/10.5194/acp-20-915-2020>,
721 2020.

722 Gysel, M., Mcfiggans, G. B., Coe, H.: Inversion of tandem differential mobility
723 analyser (TDMA) measurements, *Journal of Aerosol Science.*, 40(2), 134–151,
724 <https://doi.org/10.1016/j.jaerosci.2008.07.013>, 2009.

725 Hughes, M., Kodros, J. K., Pierce, J. R., West, M., Riemer, N.: Machine learning to
726 predict the global distribution of aerosol mixing state metrics, *Atmosphere.*, 9(1),
727 15, <https://doi.org/10.3390/atmos9010015>, 2018.

728 Huang, R. J., Zhang, Y., Bozzetti, C., Ho, K. F., Cao, J. J., Han, Y., Daellenbach, K. R.,
729 Slowik, J. G., Platt, S. M., Canonaco, F., Zotter, P., Wolf, R., Pieber, S. M., Bruns,
730 E. A., Crippa, M., Ciarelli, G., Piazzalunga, A., Schwikowski, M., Abbaszade, G.,
731 Schnelle-Kreis, J., Zimmermann, R., An, Z., Szidat, S., Baltensperger, U., Haddad,
732 I. E., Prévôt, A. S.: High secondary aerosol contribution to particulate pollution
733 during haze events in China, *Nature.*, 514(7521), 218–222, [https://doi.org/](https://doi.org/10.1038/nature13774)
734 [10.1038/nature13774](https://doi.org/10.1038/nature13774), 2014.

735 IPCC. Summary for Policymakers. In *Climate Change 2021: The Physical Science*
736 *Basis. Contribution of Working Group I to the Sixth Assessment Report of the*
737 *Intergovernmental Panel on Climate Change; Cambridge University Press:*
738 *Cambridge, United Kingdom and New York, NY, USA, 2021.*

739 Liu, P., Song, M., Zhao, T., Gunthe, S. S., Ham, S., He, Y., Qin, Y., Gong, Z., Amorim,
740 C. J., Bertram, K. A., Martin, S. T.: Resolving the mechanisms of hygroscopic
741 growth and cloud condensation nuclei activity for organic particulate matter,
742 *Nature communications.*, 9(1), 4076, [https://doi.org/10.1038/s41467-018-06622-](https://doi.org/10.1038/s41467-018-06622-2)
743 [2](https://doi.org/10.1038/s41467-018-06622-2), 2018.

744 Liu, J., Zhang, F., Ren, J., Chen, L., Zhang, A., Wang, Z., Zou, S., Xu, H., Yue, X.: The
745 evolution of aerosol mixing state derived from a field campaign in Beijing:
746 implications for particle aging timescales in urban atmospheres, *Atmospheric*
747 *Chemistry and Physics.*, 25(9), 5075–5086, [https://doi.org/10.5194/acp-25-5075-](https://doi.org/10.5194/acp-25-5075-2025)
748 [2025](https://doi.org/10.5194/acp-25-5075-2025), 2025.

749 Liu, Y., Lin, T., Zhang, J., Wang, F., Huang, Y., Wu, X., Ye, H., Zhang, G., Cao, X., and
750 de Leeuw, G.: Opposite effects of aerosols and meteorological parameters on

751 warm clouds in two contrasting regions over eastern China, *Atmospheric*
752 *Chemistry and Physics.*, 24, 4651–4673, [https://doi.org/10.5194/acp-24-4651-](https://doi.org/10.5194/acp-24-4651-2024)
753 2024, 2024.

754 Lance, S., Nenes, A., Medina, J., Smith, J. N.: Mapping the operation of the DMT
755 continuous flow CCN counter, *Aerosol Science and Technology.*, 40(4), 242–254,
756 <https://doi.org/10.1080/02786820500543290>, 2006.

757 Manavi, S. E. I., Aktypis, A., Siouti, E., Skyllakou, K., Myriokefalitakis, S., Kanakidou,
758 M., Pandis, S. N.: Atmospheric aerosol spatial variability: Impacts on air quality
759 and climate change, *One Earth.*, 8(3),
760 <https://doi.org/10.1016/j.oneear.2025.101237>, 2025.

761 Ovadnevaite, J., Ceburnis, D., Leinert, S., Dall'Osto, M., Canagaratna, M., O'Doherty,
762 S., Berresheim, H., O'Dowd, C.: Submicron NE Atlantic marine aerosol chemical
763 composition and abundance: Seasonal trends and air mass categorization, *Journal*
764 *of Geophysical Research: Atmospheres.*, 119, 11850–11863,
765 <https://doi.org/10.1002/2013JD021330>, 2014.

766 Petters, M. D., Kreidenweis, S. M.: A single parameter representation of hygroscopic
767 growth and cloud condensation nucleus activity, *Atmospheric Chemistry and*
768 *Physics.*, 7(8), 1961–1971, <https://doi.org/10.5194/acp-7-1961-2007>, 2007.

769 Padró, L. T., Moore, R. H., Zhang, X., Rastogi, N., Weber, R. J., and Nenes, A.: Mixing
770 state and compositional effects on CCN activity and droplet growth kinetics of
771 size-resolved CCN in an urban environment, *Atmospheric Chemistry and Physics.*,
772 2012, 12, 10239–10255, <https://doi.org/10.5194/acp-12-10239-2012>, 2012.

773 Rosenfeld, D., Zhu, Y., Wang, M., Zheng, Y., Goren, T., Yu, S.: Aerosol- driven droplet
774 concentrations dominate coverage and water of oceanic low-level clouds, *Science.*,
775 363(6427), <https://doi.org/10.1126/science.aay4194>, 2019.

776 Riemer, N., Ault, A. P., West, M., Craig, R. L., Curtis, J. H.: Aerosol mixing state:
777 Measurements, modeling, and impacts, *Reviews of Geophysics.*, 57(2), 187–249,
778 <https://doi.org/10.1029/2018RG000615>, 2019.

779 Ren, J., Zhang, F., Wang, Y., Collins, D., Fan, X., Jin, X., Xu, W., Sun, Y., Cribb, M.,
780 Li, Z.: Using different assumptions of aerosol mixing state and chemical
781 composition to predict CCN concentrations based on field measurements in urban
782 Beijing, *Atmospheric Chemistry and Physics.*, 18(9), 6907–6921,
783 <https://doi.org/10.5194/acp-18-6907-2018> 2018.

784 Ramachandran, S., Srivastava, R.: Mixing states of aerosols over four environmentally
785 distinct atmospheric regimes in Asia: coastal, urban, and industrial locations
786 influenced by dust, *Environmental Science and Pollution Research.*, 23, 11109–
787 11128, <https://doi.org/10.1007/s11356-016-6254-8>, 2016.

788 Ren, J., Zhang, F., Chen, L., Cao, G., Liu, M., Li, X., Wu, H., Cheng, Y., and Li, Z.:
789 Identifying the hygroscopic properties of fine aerosol particles from diverse
790 sources in urban atmosphere and the applicability in prediction of cloud nuclei,
791 *Atmos. Environ.*, 298, 119615, <https://doi.org/10.1016/j.atmosenv.2023.119615>,
792 2023.

793 Riemer, N. and West, M.: Quantifying aerosol mixing state with entropy and diversity
794 measures, *Atmospheric Chemistry and Physics.*, 13, 11423–11439,
795 <https://doi.org/10.5194/acp-13-11423-2013>, 2013.

796 Rose, D., Gunthe, S. S., Mikhailov, E., Frank, G. P., Dusek, U., Andreae, M. O., Pöschl,
797 U.: Calibration and measurement uncertainties of a continuous-flow cloud
798 condensation nuclei counter (DMT-CCNC): CCN activation of ammonium sulfate
799 and sodium chloride aerosol particles in theory and experiment, *Atmospheric
800 Chemistry and Physics.*, 8(5), 1153–1179, [https://doi.org/10.5194/acp-8-1153-](https://doi.org/10.5194/acp-8-1153-2008)
801 2008, 2008.

802 Shrivastava, M., Cappa, C. D., Fan, J., Goldstein, A. H., Guenther, A. B., Jimenez, J.
803 L., Kuang, C., Laskin, A., Martin, S. T., Ng, N. L., Petaja, T., Pierce, J. R., Rasch,
804 P. J., Roldin, P., Seinfeld, J. H., Shilling, J., Smith, J. N., Thornton, J. A., Volkamer,
805 R., Wang, J., Worsnop, D. R., Zaveri, R. A., Zelenyuk, A., Zhang, Q.: Recent
806 advances in understanding secondary organic aerosol: Implications for global
807 climate forcing, *Reviews of Geophysics.*, 55(2), 509–559,

808 <https://doi.org/10.1002/2016RG000540>, 2017.

809 Stevens, R., and Dastoor, A.: A Review of the Representation of Aerosol Mixing State
810 in Atmospheric Models, *Atmosphere.*, 10, 168,
811 <https://doi.org/10.3390/atmos10040168>, 2019.

812 Spitieri, C., Gini, M., Gysel-Beer, M., and Eleftheriadis, K.: Annual cycle of
813 hygroscopic properties and mixing state of the suburban aerosol in Athens, Greece,
814 *Atmospheric Chemistry and Physics.*, 23, 235–249, [https://doi.org/10.5194/acp-](https://doi.org/10.5194/acp-23-235-2023)
815 [23-235-2023](https://doi.org/10.5194/acp-23-235-2023), 2023.

816 Sotiropoulou, R. E. P., Nenes, A., Adams, P. J., Seinfeld, J. H.: Cloud condensation
817 nuclei prediction error from application of Köhler theory: Importance for the
818 aerosol indirect effect, *Journal of Geophysical Research: Atmospheres.*, 112(D12),
819 <https://doi.org/10.1029/2006JD007834>, 2007.

820 Schill, S. R., Collins, D. B., Lee, C., Morris, H. S., Novak, G. A., Prather, K. A., Quinn,
821 P. K., Sultana, C. M., Tivanski, A. V., Zimmermann, K., Cappa, C. D., Bertram, T.
822 H.: The impact of aerosol particle mixing state on the hygroscopicity of sea spray
823 aerosol, *ACS central science.*, 1(3), 132-141,
824 <https://doi.org/10.1021/acscentsci.5b00174>, 2015.

825 Shi, Z., Vu, T., Kotthaus, S., Harrison, R. M., Grimmond, S., Yue, S., Zhu, T., Lee, J.,
826 Han, Y., Demuzere, M., Dunmore, R. E., Ren, L., Liu, D., Wang, Y., Wild, O.,
827 Allan, J., Acton, W. J., Barlow, J., Barratt, B., Beddows, D., Bloss, W. J., Calzolari,
828 G., Carruthers, D., Carslaw, D. C., Chan, Q., Chatzidiakou, L., Chen, Y., Crilley,
829 L., Coe, H., Dai, T., Doherty, R., Duan, F., Fu, P., Ge, B., Ge, M., Guan, D.,
830 Hamilton, J. F., He, K., Heal, M., Heard, D., Hewitt, C. N., Hollaway, M., Hu, M.,
831 Ji, D., Jiang, X., Jones, R., Kalberer, M., Kelly, F. J., Kramer, L., Langford, B.,
832 Lin, C., Lewis, A. C., Li, J., Li, W., Liu, H., Liu, J., Loh, M., Lu, K., Lucarelli, F.,
833 Mann, G., McFiggans, G., Miller, M. R., Mills, G., Monk, P., Nemitz, E., O'Connor,
834 F., Ouyang, B., Palmer, P. I., Percival, C., Popoola, O., Reeves, C., Rickard, A. R.,
835 Shao, L., Shi, G., Spracklen, D., Stevenson, D., Sun, Y., Sun, Z., Tao, S., Tong, S.,
836 Wang, Q., Wang, W., Wang, X., Wang, X., Wang, Z., Wei, L., Whalley, L., Wu, X.,

837 Wu, Z., Xie, P., Yang, F., Zhang, Q., Zhang, Y., Zhang, Y., and Zheng, M.:
838 Introduction to the special issue “In-depth study of air pollution sources and
839 processes within Beijing and its surrounding region (APHH-Beijing)”,
840 *Atmospheric Chemistry and Physics*, 19, 7519–7546, [https://doi.org/10.5194/acp-](https://doi.org/10.5194/acp-19-7519-2019)
841 [19-7519-2019](https://doi.org/10.5194/acp-19-7519-2019), 2019.

842 Stokes, R. H., Robinson, R. A.: Interactions in aqueous nonelectrolyte solutions. I.
843 Solute-Solvent equilibria, *Journal of Physical Chemistry*, 70(7), 2126–2130,
844 <https://doi.org/10.1021/j100879a010>, 1966.

845 Tao, J., Kuang, Y., Ma, N., Hong, J., Sun, Y., Xu, W., Zhang, Y., He, Y., Luo, Q., Xie,
846 L., Su, H., and Cheng, Y.: Secondary aerosol formation alters CCN activity in the
847 North China Plain, *Atmospheric Chemistry and Physics*, 21, 7409–7427,
848 <https://doi.org/10.5194/acp-21-7409-2021>, 2021.

849 Tao, J., Luo, B., Xu, W., Zhao, G., Xu, H., Xue, B., Zhai, M., Xu, W., Zhao, H., Ren,
850 S., Zhou, G., Liu, L., Kuang, Y., and Sun, Y.: Markedly different impacts of
851 primary emissions and secondary aerosol formation on aerosol mixing states
852 revealed by simultaneous measurements of CCNC, H(V)TDMA, and SP2,
853 *Atmospheric Chemistry and Physics*, 24, 9131–9154, [https://doi.org/10.5194/acp-](https://doi.org/10.5194/acp-24-9131-2024)
854 [24-9131-2024](https://doi.org/10.5194/acp-24-9131-2024), 2024.

855 Virtanen, A., Joutsensaari, J., Kokkola, H., Partridge, G. D., Blichner, S., Seland, Ø.,
856 Holopainen, E., Tovazzi, E., Lipponen, A., Mikkonen, S., Leskinen, A., Hyvärinen,
857 A., Zieger, P., Krejci, R., Ekman, A. M. L., Riipinen, I., Quaas, J., Romakkaniemi,
858 S.: High sensitivity of cloud formation to aerosol changes, *Nature Geoscience*, 1–
859 7, <https://doi.org/10.1038/s41561-025-01662-y>, 2025.

860 Winkler, P.: The growth of atmospheric aerosol particles as a function of the relative
861 humidity—II. An improved concept of mixed nuclei, *Journal of Aerosol Science*,
862 4(5), 373–387, [https://doi.org/10.1016/0021-8502\(73\)90027-X](https://doi.org/10.1016/0021-8502(73)90027-X), 1973.

863 Wang, J., Cubison, M. J., Aiken, A. C., Jimenez, J. L., Collins, D. R.: The importance
864 of aerosol mixing state and size-resolved composition on CCN concentration and
865 the variation of the importance with atmospheric aging of aerosols, *Atmospheric*

866 Chemistry and Physics., 10(15), 7267–7283, <https://doi.org/10.5194/acp-10-7267->
867 2010, 2010.

868 Wang, Y., Li, Z., Zhang, R., Jin, X., Xu, W., Fan, X., et al.: Distinct ultrafine- and
869 accumulation-mode particle properties in clean and polluted urban environments,
870 Geophysical Research Letters., 46, 10,918–10,925,
871 <https://doi.org/10.1029/2019GL084047>, 2019.

872 Xu, W., Ovadnevaite, J., Fossum, K. N., Lin, C., Huang, R. J., Ceburnis, D., O’Dowd,
873 C.: Sea spray as an obscured source for marine cloud nuclei, Nature Geoscience.,
874 15(4), 282–286, <https://doi.org/10.1038/s41561-022-00917-2>, 2022.

875 Xu, W., Ovadnevaite, J., Fossum, K. N., Huang, R. J., Huang, D., Zhong, H., Gu, Y.,
876 Lin, C., Huang, C., O’Dowd, C., Ceburnis, D.: Condensation of organic-inorganic
877 vapours governs the production of ultrafine secondary marine cloud nuclei,
878 Communications Earth & Environment., 5(1), 359,
879 <https://doi.org/10.1038/s43247-024-01519-z>, 2024.

880 Xu, W., Ovadnevaite, J., Fossum, K. N., Lin, C., Huang, R. J., O’Dowd, C., Ceburnis,
881 D.: Aerosol hygroscopicity and its link to chemical composition in the coastal
882 atmosphere of Mace Head: marine and continental air masses, Atmospheric
883 Chemistry and Physics., 20(6), 3777–3791, <https://doi.org/10.5194/acp-20-3777->
884 2020, 2020.

885 Xu, W., Ovadnevaite, J., Fossum, K. N., Lin, C., Huang, R.-J., O’Dowd, C., Ceburnis,
886 D.: Seasonal trends of aerosol hygroscopicity and mixing state in clean marine and
887 polluted continental air masses over the Northeast Atlantic, Journal of Geophysical
888 Research: Atmospheres., 126, e2020JD033851,
889 <https://doi.org/10.1029/2020JD033851>, 2021a.

890 Xu, W., Sun, Y., Wang, Q., Zhao, J., Wang, J., Ge, X., Xie, C., Zhou, W., Du, W., Li, J.,
891 Fu, P., Wang, Z., Worsnop, D. R., Coe, H.: Changes in aerosol chemistry from
892 2014 to 2016 in winter in Beijing: Insights from high-resolution aerosol mass
893 spectrometry, Journal of Geophysical Research: Atmospheres., 124, 1132–1147,
894 <https://doi.org/10.1029/2018JD029245>, 2019.

895 Xie, C., He, Y., Lei, L., Zhou, W., Liu, J., Wang, Q., Xu, W., Qiu, Y., Zhao, J., Sun, J.,
896 Li, L., Li, M., Zhou, Z., Fu, P., Wang, Z., Sun, Y.: Contrasting mixing state of black
897 carbon-containing particles in summer and winter in Beijing, *Environmental*
898 *Pollution.*, 263, 114455, <https://doi.org/10.1016/j.envpol.2020.114455>, 2020.

899 Xu, W., Fossum, K. N., Ovadnevaite, J., Lin, C., Huang, R. J., O'Dowd, C., Ceburnis,
900 D.: The impact of aerosol size-dependent hygroscopicity and mixing state on the
901 cloud condensation nuclei potential over the north-east Atlantic, *Atmospheric*
902 *Chemistry and Physics.*, 21(11), 8655–8675, [https://doi.org/10.5194/acp-21-8655-](https://doi.org/10.5194/acp-21-8655-2021)
903 2021, 2021b.

904 Ye, Q., Gu, P., Li, H. Z., Robinson, E. S., Lipsky, E. M., Kaltsonoudis, C., Lee, A. K.
905 Y., Apte, J. S., Robinson, A. L., Sullivan, R. C., Presto, A. A., Donahue, N. M.:
906 Spatial variability of sources and mixing state of atmospheric particles in a
907 metropolitan area, *Environmental Science & Technology.*, 52, 6807–6815,
908 <https://doi.org/10.1021/acs.est.8b01011>, 2018.

909 Yuan, L., and Zhao, C.: Quantifying particle-to-particle heterogeneity in aerosol
910 hygroscopicity, *Atmospheric Chemistry and Physics.*, 23, 3195–3205,
911 <https://doi.org/10.5194/acp-23-3195-2023>, 2023.

912 Yang, F., Chen, H., Du, J., Yang, X., Gao, S., Chen, J., Geng, F.: Evolution of the mixing
913 state of fine aerosols during haze events in Shanghai, *Atmospheric Research.*, 104:
914 193-201, <https://doi.org/10.1016/j.atmosres.2011.10.005>, 2012.

915 Zheng, Z., Curtis, J. H., Yao, Y., Gasparik, J. T., Anantharaj, V. G., Zhao, L., West, M.,
916 Riemer, N.: Estimating submicron aerosol mixing state at the global scale with
917 machine learning and Earth system modeling, *Earth and Space Science.*, 8(2),
918 e2020EA001500, <https://doi.org/10.1029/2020EA001500>, 2021a.

919 Zheng, Z., West, M., Zhao, L., Ma, P.-L., Liu, X., and Riemer, N.: Quantifying the
920 structural uncertainty of the aerosol mixing state representation in a modal model,
921 *Atmospheric Chemistry and Physics.*, 21, 17727–17741,
922 <https://doi.org/10.5194/acp-21-17727-2021> , 2021b.

923 Zhao, G., Tan, T., Zhu, Y., Hu, M., and Zhao, C.: Method to quantify black carbon

924 aerosol light absorption enhancement with a mixing state index, *Atmospheric*
925 *Chemistry and Physics.*, 21, 18055–18063, [https://doi.org/10.5194/acp-21-18055-](https://doi.org/10.5194/acp-21-18055-2021)
926 2021, 2021.

927 Zdanovskii, A.: New methods for calculating solubilities of electrolytes in
928 multicomponent systems, *Zh. Fiz. Khim. C*, 22, 1475–1485, 1948.

929 Zhong, H., Huang, R. J., Lin, C., Xu, W., Duan, J., Gu, Y., Huang, W., Ni, H.; Zhu, C.,
930 You, Y., Wu, Y., Zhang, R., Ovadnevaite, J., Ceburnis, D., O'Dowd, C.:
931 Measurement report: On the contribution of long-distance transport to the
932 secondary aerosol formation and aging, *Atmospheric Chemistry and Physics.*, 22,
933 9513–9524, <https://doi.org/10.5194/acp-22-9513-2022>, 2022.